Annals of Biomedical Engineering, Vol. 25, pp. 547–564, 1997
Printed in the USA. All rights reserved.

0090–6964/97 $10.50 + .00

Efficient Numerical Methods for Nonlinear-Facilitated Transport and Exchange in a Blood-Tissue Exchange Unit

CHRISTOPHE A. POULAIN,* BRUCE A. FINLAYSON,* and JAMES B. BASSINGTHWAIGHTE†

*Department of Chemical Engineering and †Center for Bioengineering, University of Washington, Seattle, WA

Abstract—The analysis of experimental data obtained by the multiple-indicator method requires complex mathematical models for which capillary blood-tissue exchange (BTEX) units are the building blocks. This study presents a new, nonlinear, two-region, axially distributed, single capillary, BTEX model. A facilitated transporter model is used to describe mass transfer between plasma and intracellular spaces. To provide fast and accurate solutions, numerical techniques suited to nonlinear convection-dominated problems are implemented. These techniques are the random choice method, an explicit Euler-Lagrange scheme, and the MacCormack method with and without flux correction. The accuracy of the numerical techniques is demonstrated, and their efficiencies are compared. The random choice, Euler-Lagrange and plain MacCormack method are the best numerical techniques for BTEX modeling. However, the random choice and Euler-Lagrange methods are preferred over the MacCormack method because they allow for the derivation of a heuristic criterion that makes the numerical methods stable without degrading their efficiency. Numerical solutions are also used to illustrate some nonlinear behaviors of the model and to show how the new BTEX model can be used to estimate parameters from experimental data.

Keywords—Random choice method, Euler-Lagrange method, MacCormack method, Flux-corrected transport, Capillary permeability.

INTRODUCTION

The interpretation of experimental data obtained by tracer outflow experiments relies on the availability of appropriate mathematical models. Despite evidence of the nonlinearity of many axially distributed blood-tissue exchange (BTEX) processes, few models have been proposed that describe their full dynamic behavior. A common approach to study such nonlinear processes is to infuse into the circulation a constant level of a substrate of interest and to wait for steady-state. This step is usually followed by a rapid injection of minute amounts of radiolabeled tracers. With respect to the analysis of data, such tracer experiments are advantageous because the solution to the nonlinear model equations is only needed for the steady-state. The time-dependent tracer equations are automatically linearized thanks to the assumption that the radioactive marker does not change the state of the system, because its concentration is negligible in comparison with the background concentration of nontracer substrate. The problem with this experimental method is that it only provides information on the system at a particular state. To understand the nonlinear behavior of the processes, it is necessary to do several experiments to obtain steady-state concentrations that span the entire nonlinear range. However, long constant infusions of high doses of substrate are problematic *in vivo,* because they can jeopardize the life of the organ under investigation or modify its physiological state to an extent such that the experiment is no longer relevant. To avoid the aforementioned difficulties, Malcorps *et al.* (22) have developed the "bolus sweep" technique (see Ref. 22 for a discussion of this technique *versus* constant-infusion techniques). This procedure consists of a rapid injection of a bolus containing both radiolabeled substrate and a sufficient amount of nontracer substrate to sweep the nonlinear range of concentration. Therefore, one experiment brings enough information to estimate the actual parameters of a nonlinear model. On the other hand, data from "bolus sweep" experiments are more difficult to analyze, in particular, because they require the capability to solve complicated, nonlinear, time-dependent models.

The present study introduces a new, two-region, axially distributed BTEX model with nonlinear facilitated transport and reaction. The aim of this study is to present the methods that will serve for the development of more sophisticated nonlinear models. Therefore, emphasis is put not as much on the model itself as on the means used to solve it and to analyze experimental data with it. The model solutions are obtained with three numerical tech-

Acknowledgment—We thank one of the referees for suggestions on how to differentiate between dispersion due to different transit times and dispersion due to axial diffusion. Support has been provided by the National Institutes of Health, National Center for Research Resources, through Grant RR 1243 to the Simulation Resource in Mass Transport and Exchange. See the Web site at nsr.bioeng.washington.edu. C. A. Poulain's current address is Aspen Technology, Inc., 10 Canal Park, Cambridge, MA 02141.

Address correspondence to Bruce A. Finlayson, Department of Chemical Engineering, Mail Stop BF-10, University of Washington, Seattle, WA 98195, U.S.A.

(Received 14Aug95, Revised 17Jul96, Revised, Accepted 15Aug96)

niques suited to nonlinear convection-dominated problems. The three methods are presented and compared in terms of their numerical efficiency—which represents the trade-off between accuracy and computational speed—and robustness. Once we have established the capabilities of the numerical methods, we proceed to show some general features of the new nonlinear model. We conclude by demonstrating how parameters of the model can be reliably estimated from simulated data with noise.

THE NONLINEAR AXIALLY DISTRIBUTED TWO-REGION BTEX UNIT

The two-region, axially distributed BTEX unit is shown in Fig. 1. It is a Krogh tissue cylinder consisting of two regions (plasma and intracellular spaces) separated by one barrier. When the effects of convection, axial diffusion, permeation, and consumption are included, the spatial and temporal variations of concentration C of a substrate S in the intra- and extravascular spaces are described by two partial differential equations. In the plasma space, p:

$$\frac{\partial C_p}{\partial t} = -\frac{F_p L}{V_p}\frac{\partial C_p}{\partial x} - \frac{PS_{p\to c} + G_p}{V_p} C_p + \frac{PS_{c\to p}}{V_p} C_c + D_p \frac{\partial^2 C_p}{\partial x^2}. \quad (1)$$

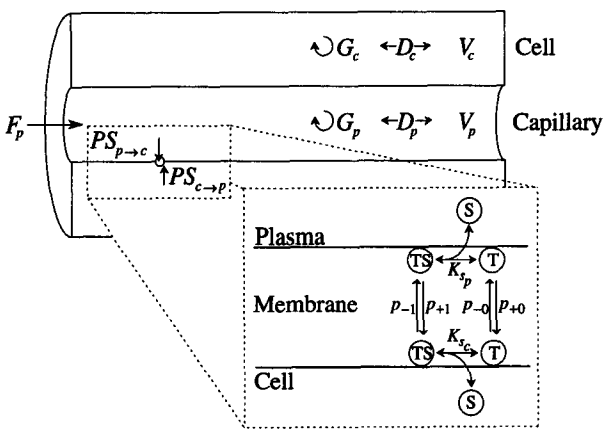

FIGURE 1. A model for a two-region, axially distributed BTEX unit with facilitated transport. (Background) The capillary is composed of two concentric cylindrical regions separated by one barrier. Subscripts are *p* for plasma and *c* for intracellular space. F_p = *plasma flow rate;* V = volume; D = axial diffusion coefficient; G = rate of consumption; PS = permeability-surface area products. (Foreground) Permeabilities across the barrier are determined by the transporter model. Circled S, T, and TS represents free substrate molecule, free transporter molecule, and transporter-substrate complex, respectively. At each side of the membrane, the three species are in equilibrium. Only free transporter and complex molecules can "diffuse" across the membrane wall. K_s = binding equilibrium constant; p_{+1} = permeability for transporter-substrate complex from plasma to tissue; p_{-1} = permeability for transporter-substrate complex from tissue to plasma; p_{+0} and p_{-0} are similar quantities for free transporter.

In the intracellular region, c:

$$\frac{\partial C_c}{\partial t} = +\frac{PS_{p\to c}}{V_c} C_p - \frac{PS_{c\to p} + G_c}{V_c} C_c + D_c \frac{\partial^2 C_c}{\partial x^2}. \quad (2)$$

The auxiliary conditions associated with these equations are at the initial time t_0:

$$C_p(x, t_0) = C_c(x, t_0) = C_0 \quad \text{for} \quad 0 \le x \le L, \quad (3)$$

and at the boundaries:

$$C_p(0, t) = C_{in}(t) \quad \text{and} \quad \left.\frac{\partial C_p}{\partial x}\right|_{x=L,t} = \left.\frac{\partial C_c}{\partial x}\right|_{x=0,t}$$

$$= \left.\frac{\partial C_c}{\partial x}\right|_{x=L,t} = 0 \quad \text{for} \quad t_0 < t. \quad (4)$$

The derivation of Eqs. 1 and 2 assumes constant piston flow in the capillary and negligible radial concentration gradients in both regions. These assumptions and the choice of boundary conditions have been discussed in detail by Bassingthwaighte *et al.* (4).

Facilitated Transporter

The model incorporates a nonlinear facilitated transporter for radial exchanges. As a result, the permeability-surface area products are concentration-dependent. Figure 1 shows a diagram of the nonlinear transporter. To describe it, four new quantities are introduced: T_p and T_c denote the surface concentration of free transporter T with binding site facing the plasma region and the intracellular region, respectively. TC_p and TC_c stand for the surface concentration of transporter-substrate complex TS facing plasma and intracellular space, respectively. Each of these quantities can be expressed in moles per membrane surface area or, when multiplied by the ratio membrane surface area to gram of tissue, in moles per gram. With this notation, the facilitated transporter is characterized by:

(a) The total number of transporter sites per unit membrane surface area:

$$T_T = T_p + TC_p + T_c + TC_c.$$

To reflect the conservation of the total number of transporter molecules, T_T is constant at any fixed position along the capillary. In the present work, it is also assumed that the axial distribution of transporter total surface concentration is uniform, so that T_T takes a unique value over the entire exchange unit.

(b) The rates of permeation across the membrane for free transporter and transporter-substrate complex: During active transport, radial mass transfer occurs because bound and unbound transporters have the ability to translocate the active site on the transporter protein from one side of

the membrane to the other. Although the process of translocation is not completely understood, it implies a conformational change in the membrane spanning (or integral) protein, and it can be modeled with effective permeation rate constants. In Fig. 1, p_{+1} and p_{-1} denote the rate at which the transporter-substrate complex flips or translocates the substrate binding site in the direction from plasma to cell and from cell to plasma, respectively. p_{+0} and p_{-0} are similar quantities for free transporter. The p's are in units of inverse seconds.

(c) The mechanism of association and dissociation between transporter and substrate molecules: Free substrate molecules, S, and transporter molecules, T, combine in a one-to-one relationship to form a complex, TS. The binding reaction is of first-order with respect to each reactant and is reversible:

$$\mathrm{T} + \mathrm{S} \underset{k_r^-}{\overset{k_r^+}{\rightleftarrows}} \mathrm{TS},$$

with rates of formation at the plasma and cell side of the barrier being, respectively,

$$\frac{dTC_p}{dt} = k_p^+ T_p \bullet C_p - k_p^- TC_p \quad \text{and} \quad \frac{dTC_c}{dt} = k_c^+ T_c \bullet C_c - k_c^- TC_c.$$

To define the facilitated transporter completely, two additional assumptions are made. First, association and dissociation of substrate and transporter are assumed to be very fast, compared with radial transport events. Therfore, free substrate and transporter and transporter-substrate complex seem to be in continuous equilibrium at each side of the membrane. The binding mechanism is then described by the affinity constants:

$$K_{s_p} = \frac{k_p^-}{k_p^+} = \frac{C_p \bullet T_p}{TC_p} \quad \textit{and} \quad K_{s_c} = \frac{k_c^-}{k_c^+} = \frac{C_c \bullet T_c}{TC_c} \tag{5}$$

at the plasma–membrane interface and at the membrane–cell interface, respectively. Although this first assumption is equivalent to the quasiequilibrium hypothesis of Michaelis and Menten (23), the second assumption is comparable with the quasi-steady-state approach of Briggs and Haldane (7). It is assumed that the surface concentration of transporter (free and bound) molecules at one side of the membrane always reaches steady-state very rapidly. Therefore:

$$\frac{d(T_p + TC_p)}{dt} = \frac{d(T_c + TC_c)}{dt} = 0. \tag{6}$$

Notice that the quantities $T_p + TC_p$ and $T_c + TC_c$ are not in a true steady-state, because their values change in response to a perturbation in C_p or C_c. However, the changes in $T_p + TC_p$ and $T_c + TC_c$ occur so rapidly that these two quantities can be regarded as in steady-state with respect to the instantaneous values of C_p or C_c.

Equation 5 combined with the conservation of total transporter sites, and Eq. 6 provides two relations between T_p and T_c:

$$\delta_p T_p + \delta_c T_c = T_T \quad \text{and} \quad \gamma_p T_p = \gamma_c T_c, \tag{7}$$

where

$$\delta_p = 1 + \frac{C_p}{K_{s_p}}, \ \delta_c = 1 + \frac{C_c}{K_{s_c}}, \ \gamma_p = p_{+0} + p_{+1}\frac{C_p}{K_{s_p}}, \quad \text{and} \quad \gamma_c = p_{-0} + p_{-1}\frac{C_c}{K_{s_c}}.$$

Solving for free transporter surface concentrations and noting that the fluxes of substrate from plasma to cell and from cell to plasma are, respectively,

$$\mathcal{J}_{p\to c} = p_{+1}\, TC_p \quad \text{and} \quad \mathcal{J}_{c\to p} = p_{-1}\, TC_c,$$

one easily gets the permeability-surface area products:

$$PS_{p\to c} = \frac{\gamma_c T_T p_{+1}}{(\gamma_c \delta_p + \gamma_p \delta_c) K_{s_p}} \quad \text{and}$$

$$PS_{c\to p} = \frac{\gamma_p T_T p_{-1}}{(\gamma_c \delta_p + \gamma_p \delta_c) K_{s_c}}. \tag{8}$$

It is always possible to express the PS's above in terms of an apparent maximal transport rate via the transporter, V_{max}, and an apparent Michaelis constant, K_m, to show the equations in the form commonly used for first order Michaelis-Menten reactions. For example, one might write $PS_{p\to c} = V'_{max_p}/(K'_{m_p} + C_p)$ with:

$$V'_{max_p} = T_T p_{+1} \frac{\gamma_c}{\gamma_c + p_{+1}\delta_c} \quad \text{and} \quad K'_{m_p} = K_{s_p} \frac{\gamma_c + p_{+0}\delta_c}{\gamma_c + p_{+1}\delta_c}. \tag{9}$$

Similarly, one could define for $PS_{c\to p}$:

$$V'_{max_c} = T_T p_{-1} \frac{\gamma_p}{\gamma_p + p_{-1}\delta_p} \quad \text{and} \quad K'_{m_c} = K_{s_c} \frac{\gamma_p + p_{-0}\delta_p}{\gamma_p + p_{-1}\delta_p}. \tag{10}$$

Notice that the quantities defined by Eqs. 9 and 10 depend on C_c and C_p. However, they are constant when $p_{+0} = p_{-0} = p_{+1} = p_{-1} = p$, which shows that the present transporter model is a generalization of Michaelis-Menten kinetics. The expressions of Eqs. 9 and 10 are compact in the sense that they group individual parameters of the transporter model. As we shall see in a later section dealing with the analysis of experimental data, this compactness sometimes proves useful when not all parameters of the model are distinguishable. In addition, the calcula-

tion of V_{max} and K_m should facilitate comparison with existing results involving Michaelis-Menten kinetics.

Reaction Kinetics

The BTEX unit also accounts for consumption of substrate within each region, subscripted *r*. Two first-order, irreversible processes are available to model the removal of substrate:

$$G_r = G_{\max_r} \quad \text{or} \quad G_r = \frac{V_{\max_r}}{K_{mr} + C_r}, \quad r = c \text{ or } p.$$

Only the first scheme is linear. The second scheme corresponds to Michaelis-Menten kinetics, and this one is used to derive the time-step limits.

Tracer and Nontracer Substrates

Linear BTEX models are not necessarily inappropriate for the analysis of processes, wherein permeation and consumption parameters are actually concentration-dependent (see p. 560 of Ref. 2;14,17,19). However, the linearity of parameters requires that plasma and tissue concentrations of nontracer "mother" substrate be effectively uniform. Of course, this approximation will likely be wrong when substrate is consumed and is inadequate for the analysis of indicator-dilution experiments using rapid injection into the blood of bolus containing both labeled and unlabeled substrate (22).

The nonlinear model presented herein accounts for axial gradients in nontracer concentration. To account for the most general situations, two systems of equations are solved simultaneously. The first system is given by Eqs. 1 to 4 and yields the nontracer concentrations C_p and C_c. The second system is obtained by replacing C_p and C_c in Eqs. 1 to 4 by the corresponding tracer concentrations C_p^* and C_c^*. For both systems of equations, exchange and consumption parameters are function of the quantities $C_p^{tot} = C_p + C_p^*$ and $C_c^{tot} = C_c + C_c^*$, which, by defining a tracer to be at a molar concentration level negligible compared with that of the nontracer mother substance, reduce to C_p and C_c, respectively.

NUMERICAL METHODS OF SOLUTION

The solution of general nonlinear models requires the use of numerical techniques. As shown by Bassingthwaighte *et al.* (4), the latter can advantageously replace analytical solutions for the modeling of BTEX. In particular, numerical techniques offer superior flexibility over analytical solutions, because slight changes in the model equations (like adding a source term or testing a new boundary condition) can often be handled by just modifying a few lines of the computer program. These advantages come with a price. First, numerical solutions are not exact due to numerical errors. Of course, the error of a convergent algorithm can be made smaller and smaller (down to the accuracy of the computer), but this gain in precision is always accompanied by a rise in computational time. Therefore, it is desirable to rate a numerical technique in terms of its efficiency (*i.e.*, by evaluating the trade-off between accuracy and speed). When using a numerical technique, one must also be aware of its stability requirements. Whereas sophisticated theories have been developed for linear problems, the stability analysis for nonlinear systems relies largely on linearization and empiricism.

In a previous work (24), we compared the efficiency of several numerical techniques for the solution of nonlinear convection-dominated problems with sharp fronts. We concluded that three methods were particularly attractive: the random choice technique, the Euler-Lagrange technique, and MacCormack method with flux correction. The following sections describe the extension of these three methods to the nonlinear, two-region BTEX model.

Random Choice Method

Recent reviews of the random choice technique applied to nonlinear convection-dominated problems are available in Holt (16) and Finlayson (12). For the present BTEX unit, the random choice method is applied in two steps. In the first step, the plasma advective term is removed from the model equations, which are then solved to account for the effects of permeation, consumption, and axial diffusion. After that, an advection step is added in the plasma space. Note that the order of the two steps can be reversed.

In the first step of the random choice technique, Eqs. 1 and 2 are replaced by a nonlinear system of differential equations which, in matrix form; is:

$$\frac{D\mathbf{C}}{Dt} = \mathbf{B}(\mathbf{C}^{tot})\,\mathbf{C} + D\frac{\partial^2 \mathbf{C}}{\partial x^2}. \tag{11}$$

The time derivative, $D \cdot /Dt$, is a substantial derivative as explained by Bird *et al.* (p. 73 of Ref. 5). $\mathbf{C}$ is the tracer concentration, and $\mathbf{C}^{tot}$ is the total concentration. Equation 11 is solved by finite differencing from the current solution time t^n to the next time level $t^{n+1} = t^n + \Delta t$. The initial condition is given by the vector of concentrations at time t^n: $\mathbf{C}^n = (C_p^n, C_c^n)^T$. Because fast computations are desired, a first-order explicit Euler scheme is used to integrate Eq. 11, and the diffusion term is approximated with a three-point centered finite difference (12). The resulting solution is a vector with components: $\tilde{C}_p^{n+1}$ and C_c^{n+1}. The latter is the new concentration in the intracellular space, but the former is only an intermediate quantity to which the effect of convective transport must be applied.

Because the plasma velocity is constant, it is possible to

modify slightly the random choice technique to improve its speed during the advection step. With the linear advective equation, a wave is propagated unchanged at speed $u = F_p/V_p$ in the x direction. But to compute the movement of such a wave, the numerical technique approximates the continuous spatiotemporal domain by a discrete domain $\{\{i\Delta x;\ n\Delta t\} \mid i \in \{0; 1 \ldots; N_{seg}\},\ n \in \{0; 1 \ldots; N_{stp}\}\}$ and, in the numerical approximation, a wave propagating in the x direction can only advance by increment of size Δx. So, after n whole time steps, the exact solution has traveled a distance:

$$\delta_{ex}(n\Delta t) = n\, u\, \Delta t,$$

whereas the numerical solution has covered a distance of

$$\delta_{num}(n\Delta t) = k(n\Delta t)\, \Delta x,$$

where k is a positive integer depending on time. Clearly, one will obtain a good approximation to the exact solution when, at any time, the difference $\delta = \delta_{ex} - \delta_{num}$ is as small as possible and when, in addition, the time average of $\delta(t)$ is close to zero. The random choice technique uses random variables to ensure that the error δ remains in the range $[-\Delta x/2; \Delta x/2]$ and that its average over time is 0. For the linear advection equation, however, it is faster not to use random variables but still achieve the same effect. If, at time $t^n = n\Delta t$, we know $C^n_{p,i}$ the numerical approximation to $C_p(i\Delta x, n\Delta t)$ and we also have $k^n = k(n\Delta t)$ such that:

$$|u\, n\, \Delta t - k^n\, \Delta x| \leqslant \Delta x/2.$$

Then, we define the solution to the advection step at time t^{n+1} according to:

$$C^{n+1}_{p,i} =$$

$$\begin{cases} C^n_{p,i} & \text{and} \quad k^{n+1} = k^n & \text{if} \quad |ut^{n+1} - k^n\, \Delta x| < \Delta x/2 \\ C^n_{p,i-1} & \text{and} \quad k^{n+1} = k^n + 1 & \text{if} \quad |ut^{n+1} - k^n\, \Delta x| > \Delta x/2 \end{cases} \tag{12}$$

This algorithm requires that k be known at the initial time. k^0 is picked equal to 0, which means that initial and boundary conditions are assumed to coincide with the exact solution. Naturally, when the advection step is the second stage in the solution process, $\tilde{C}^{n+1}_p$ is substituted for C^n_p in Eq. 12. Finally, notice that the previously described formula implicitly assumes that the Courant number $\mathrm{Co} = u\Delta t/\Delta x$ is less than or equal to unity, which is required by the random choice method. The Courant number is how far the fluid moves in a time step compared with the grid spacing.

To reach the design goals, we also need a stability criterion for the method. A global stability analysis is extremely difficult to derive because of the nonlinearities. Nevertheless, it is possible to study the local behavior of the numerical technique using Von Neumann stability analysis in the way recommended by Fletcher (p. 162 of Ref. 13) for nonlinear equations.

For the random choice method, the convection step is always stable. Thus, the stability of the technique depends on the stability of the first stage in the solution process:

$$\begin{cases} \dfrac{\tilde{C}^{n+1}_{p,i} - C^n_{c,i}}{\Delta t} = \mathrm{RHS}_p(i;\ C^n_p;\ C^n_c) & \text{(13a)} \\ \dfrac{C^{n+1}_{c,i} - C^n_{c,i}}{\Delta t} = \mathrm{RHS}_c(i;\ C^n_p;\ C^n_c), & \text{(13b)} \end{cases}$$

where

$$\begin{cases} \mathrm{RHS}_p(i;\ C^n_p;\ C^n_c) = -\dfrac{PS_{p\to c,i} + G_{p,i}}{V_p} C^n_{p,i} \\ \qquad + \dfrac{PS_{c\to p,i}}{V_p} C^n_{c,i} \\ \qquad + \dfrac{D_p}{\Delta x^2}(C^n_{p,i+1} \\ \qquad - 2\, C^n_{p,i} + C^n_{p,i-1}) \\ \mathrm{RHS}_c(i;\ C^n_p;\ C^n_c) = +\dfrac{PS_{p\to c,i}}{Vc} C^n_{p,i} \\ \qquad - \dfrac{PS_{c\to p,i} + G_{c,i}}{Vc} C^n_{c,i} \\ \qquad + \dfrac{D_c}{\Delta x^2}(C^n_{c,i+1} \\ \qquad - 2\, C^n_{c,i} + C^n_{c,i-1}). \end{cases}$$

To overcome the mathematical difficulties created by nonlinearities, permeability-surface area products and consumption rates are temporarily "frozen". With PS's and G's being locally constant, the Von Neumann stability analysis can be applied (26). Assuming solutions to the linearized system can be written as Fourier series:

$$C_r(\xi) = \sum_{j=-\infty}^{j=+\infty} \hat{C}_{r,j}\, e^{Ij\xi} \quad (0 \leq \xi \leq 2\pi;\ r = p \text{ or } c;\ I^2 = -1), \tag{14}$$

and substituting the Fourier series for each concentration in Eq. 13 yields a relation between the Fourier coefficients at time t^{n+1} and those at the preceding time level:

$$\hat{\mathbf{C}}^{n+1} = (\mathbf{I} + \Delta t\mathbf{A})\hat{\mathbf{C}}^n. \tag{15}$$

$\mathbf{G} = \mathbf{I} + \Delta t\mathbf{A}$ is called the amplification matrix. $\mathbf{I}$ denotes the identity matrix, and $\mathbf{A}$ is given by:

$$\mathbf{A} = (a_{ij}) = \begin{bmatrix} \left(\frac{PS_{p\to c,i} + G_{p,i}}{V_p} + \frac{4D_p}{\Delta x^2}\sin^2\frac{\xi}{2}\right) & \frac{PS_{p\to c,i}}{V_c} \\ \frac{PS_{c\to p,i}}{V_p} & -\left(\frac{PS_{c\to p,i} + G_{c,i}}{V_c} + \frac{4D_c}{\Delta x^2}\sin^2\frac{\xi}{2}\right) \end{bmatrix}. \quad (16)$$

A necessary condition for stability is that both eigenvalues of the amplification matrix have a norm less than unity.

The eigenvalues are easily determined:

$$\lambda_\pm = 1 + \frac{\Delta t}{2}\left[a_{11} + a_{22} \pm \sqrt{(a_{11} - a_{22})^2 + 4a_{12}\,a_{21}}\right]. \quad (17)$$

They are real with λ_- less than or equal to λ_+. Therefore, for their values to lie in the interval between -1 and 1, two conditions must hold:

$$a_{12}\,a_{21} \le a_{11}\,a_{22} \quad (18)$$

$$\Delta t\left[-(a_{11} + a_{22}) + \sqrt{(a_{11} - a_{22})^2 + 4a_{12}\,a_{21}}\right] \le 4. \quad (19)$$

Interestingly, the first of these relations does not involve the time step.

The model is normally limited to consumption of substrate (*i.e.*, $G_r \ge 0$), and we can base the analysis on Eqs. 18 and 19. It is readily verified that, when $G_r \ge 0$, Eq. 18 always holds. Thus, Eq. 19 can be recast into the simpler form that is faster to compute (something that is useful, because the coefficients a_{ij} are usually different at each time step and at each mesh point):

$$\Delta t \le \Delta t_i = \frac{2}{\frac{PS_{p\to c,i} + G_{p,i}}{V_p} + \frac{4\,D_p}{\Delta x^2} + \frac{PS_{c\to p,i} + G_{c,i}}{V_c} + \frac{4D_c}{\Delta x^2}}, \quad (20)$$

because on one hand:

$$-(a_{11} + a_{22}) + \sqrt{(a_{11} - a_{22})^2 + 4a_{12}\,a_{21}} \le -2(a_{11} + a_{22}), \quad (21)$$

and, on the other hand, the quantity $-(a_{11} + a_{22})$—as a linear function of $\sin^2(\xi/2)$—is maximum when $\sin^2(\xi/2)$ is equal to 1.

For the present nonlinear BTEX model, Eq. 20 is tested at each node of the discrete spatial domain to automatically provide a "stable" time step $\Delta t_{\text{lim}} = \text{Min}\{\Delta t_i \mid i \in \{0; 1 \ldots; N_{\text{seg}}\}\}$ to advance the solution from the current time t to $t + \Delta t_{\text{lim}}$. This heuristic is an approximation that works well in practice to keep the solution process stable without degrading the efficiency of the numerical technique. To account for the lack of rigor in the analysis (because the coefficients are frozen at their local values), we have introduced a scaling factor, Γ, in the final stability criterion:

$$\Delta t \le \Gamma\,\Delta t_{\text{lim}}. \quad (22)$$

Γ is parameter that can be adjusted by the user of the simulation program to choose a stricter ($\Gamma < 1$) or looser ($\Gamma > 1$) way of selecting the time step used by the numerical technique. In practice, it is safer to use a time step that is slightly below the stability limit defined by Δt_{lim}. Therefore, we recommend setting Γ to a value below 1 (*e.g.*, $\Gamma = 0.9$). Nevertheless, experience shows that the model is very robust, even with Γ equal to 1. When Γ is set above that limit, the numerical scheme sometimes remains stable, but, in general, it does not. Therefore, it is wise to always keep Γ below unity.

When the reactions involve production of a species (*i.e.*, $G_r < 0$), one of the eigenvalues is always greater than 1. As explained by Richtmyer and Morton (26), the stability argument must be adjusted to allow for a "legitimate" exponential growth of the exact solution. Therefore, when substrate is produced within the BTEX unit, it is necessary to revise the stability analysis with looser requirements, namely $|\lambda \pm| \le 1 + o(\Delta t)$.

Euler-Lagrange Method

Like the random choice technique, the Euler-Lagrange technique dissociates convection from the other phenomena occurring in the exchange unit. Consequently, Eq. 11 is solved before the effect of advection is added. In the Euler-Lagrange method, however, the convection step is solved exactly because the spatial discretization of the intravascular space uses a mesh that moves along with the flowing plasma. The ensuing difficulty is that nodes of the moving mesh do not, in general, coincide with nodes of the fixed mesh, which is used in the intracellular space. Therefore, some extra work is needed to evaluate the amount of mass exchanged between regions.

Let ξ_j^n denote the abscissa of the jth node of the moving mesh at time t^n and x_i that of the ith node of the fixed mesh. Let us emphasize that, in the following discussion, discrete quantities with subscript j are known at the nodes of the moving mesh (which will be referred to as the j mesh), whereas discrete quantities with subscript i are known at the nodes of the fixed mesh (the i mesh). Figure 2 shows the concentration values available at the beginning of a time step (*e.g.*, at time t^n). At this time, we know $C_{p,j}^n$ and $C_{c,i}^n$, the numerical approximations to the concentration in the plasma at ξ_j^n and in the intracellular space at x_i, respectively.

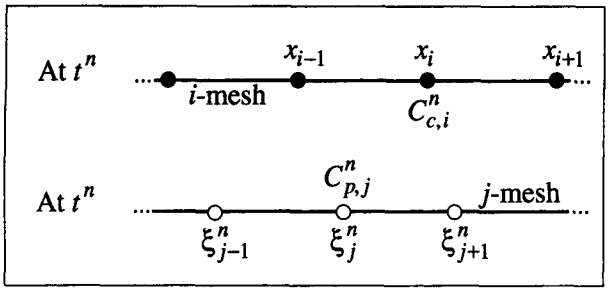

FIGURE 2. Data available at the beginning of a time step in the Euler-Lagrange method.

The key step is to calculate a solution (*e.g.*, for $C_{c,i}$) on the fixed grid when it depends on the solution (for $C_{p,j}$) on a moving grid. Interpolation back and forth is necessary. The scheme used herein was developed following Finlayson (12) with much experimentation to improve it and make it more efficient. Further details are given in Poulain (25). The Euler-Lagrange method we present is calculated two ways. In the first method, the plasma concentration is interpolated from the fixed grid to the moving grid, but the method adds excessive dispersion because piecewise linear interpolation is used. In the second method, the right-hand side of the plasma equation is interpolated from the fixed grid to the moving grid, but this method oscillates near sharp fronts when piecewise linear interpolation is used. The final method uses a combination of these two methods in such a way to avoid excessive dispersion while avoiding oscillations near sharp fronts.

In the first method (Fig. 3), one starts by interpolating values of the plasma concentration at t^n from the j mesh onto the i mesh. Then, $C^n_{p,i} = H_{C^n_{p,j}}(x_i)$, and $C^n_{c,i}$ are used to compute the new intracellular concentration on the i mesh:

$$C^{n+1}_{c,i} = C^n_{c,i} + \Delta t \mathrm{RHS}_c(i;\ C^n_p;\ C^n_c). \tag{23}$$

On this same mesh, one can also obtain an approximation of the plasma concentration at the new time with:

$$\tilde{C}^{n+1}_{p,i} = C^n_{p,i} + \Delta t \mathrm{RHS}_p(i;\ C^n_p;\ C^n_c). \tag{24}$$

Next, the value of $\tilde{C}^{n+1}_p$ are interpolated back from the i mesh onto the old j mesh. This gives the provisional quantity $\tilde{C}^{n+1}_{p,j}$ to which the effect of convection is added with

$$C^{n+1}_{p,j} = \tilde{C}^{n+1}_{p,j} \quad \text{and} \quad \xi^{n+1}_j = \xi^n_j + u\Delta t \tag{25}$$

to obtain the new plasma concentration profile along the capillary.

We applied the scheme of Fig. 3 with several types of interpolation. None gave satisfactory results in the presence of sharp plasma concentration fronts. Piecewise quadratic polynomial interpolation and cubic spline interpolation give rise to oscillations near steep axial gradients. On the other hand, piecewise linear interpolation leads to a solution that is excessively smoothed. This numerical

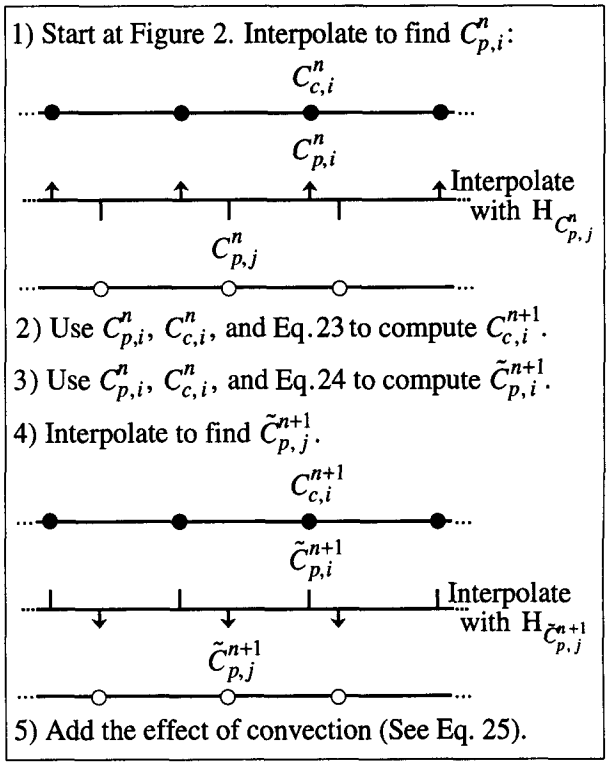

FIGURE 3. Schematic for a preliminary explicit Euler-Lagrange scheme (Eqs. 23 to 25), with cell concentration interpolated.

smearing is somewhat attenuated when higher order essentially nonoscillatory piecewise interpolation polynomials (15) are used, but solutions remain unsatisfactory.

The second scheme is presented in Fig. 4. As previously described, C^n_p is interpolated from the j mesh onto the i mesh, and a finite difference computation on the latter

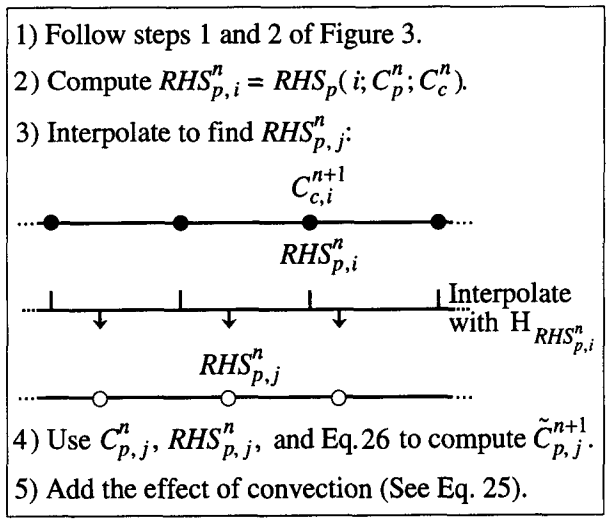

FIGURE 4. Schematic for an improved explicit Euler-Lagrange scheme (Eq. 26) with RHS interpolated.

grid yields $C_{c,i}^{n+1}$. Next, the quantity $\mathrm{RHS}_{p,i}^{n} = \mathrm{RHS}_p(i; C_p^n; C_c^n)$ is evaluated on the i mesh. Then, using an interpolating function $H_{\mathrm{RHS}_{p,i}^n}$ passing through the points of $\{\{x_i; \mathrm{RHS}_{p,i}^n\} | i = 0; 1 \ldots; N_{\mathrm{seg}}\}$, it is possible to approximate the right-hand side of Eq. 13a at each node of the j mesh: $\mathrm{RHS}_{p,j}^n = H_{\mathrm{RHS}_{p,i}^n}(\xi_j^n)$ and to compute the provisional quantity $\tilde{C}_{p,j}^{n+1}$ according to:

$$\tilde{C}_{p,j}^{n+1} = C_{p,j}^n + \Delta t \mathrm{RHS}_{p,j}^n. \tag{26}$$

The final plasma concentration is obtained after adding the convection step.

This form of the Euler-Lagrange method provides good results for sufficiently smooth solutions, but is unsatisfactory near sharp concentration fronts. Equation 26 gives rise to oscillations near steep gradients because, during the interpolation, the quantity $\mathrm{RHS}_{p,j}^n$ is grossly either under- or overestimated. This behavior occurs whether oscillatory (*i.e.*, piecewise quadratic polynomial, cubic spline) or nonoscillatory (*i.e.*, piecewise linear polynomial, high-order essentially nonoscillatory piecewise polynomial) interpolation schemes are used.

Because each of the two methods has deficiencies, we blend them as follows. We compute step 3 of Fig. 3 *and* steps 2 and 3 of Fig. 4 to obtain $\tilde{C}_{p,i}^{n+1}$ and $\mathrm{RHS}_{p,j}^n$, respectively. Piecewise linear polynomials are used for the interpolation. Now, let us denote with the subscript I the node of the i mesh, which is immediately to the left of the jth node of the moving mesh. Then, ξ_j^n belongs to the interval $[x_I; x_{I+1}]$ because, in our implementation of the Euler-Lagrange techniques, the maximum spacing on the j grid is constrained to a value no greater than the i mesh spacing to prevent any degradation of the spatial resolution. The provisional solution in the plasma is computed according to:

$$\tilde{C}_{p,j}^{n+1} = C_{p,j}^n + \Delta t \overline{\mathrm{RHS}}_{p,j}^n \tag{27}$$

with

$$M_I^{n+1} = \mathrm{Max}\{\tilde{C}_{p,I}^{n+1}; \tilde{C}_{p,I+1}^{n+1}\} \quad m_I^{n+1} = \mathrm{Min}\{\tilde{C}_{p,I}^{n+1}; \tilde{C}_{p,I+1}^{n+1}\}$$

$$\Delta \overline{\mathrm{RHS}}_{p,j}^n = \mathrm{Max}\begin{cases} \mathrm{Min}\{\Delta t \mathrm{RHS}_{p,j}^n; M_I^{n+1} - C_{p,j}^n\} \\ m_I^{n+1} - C_{p,j}^n \end{cases} \tag{28}$$

Finally, the new solution is obtained by applying the convection step of Eq. 25.

In effect, the algorithm of Eqs. 27 and 28 is limiting the amount of mass exchanged and consumed during one time step, $\Delta t \mathrm{RHS}_{p,j}^n$ (which is obtained with the scheme of Fig. 4), so as to keep the new plasma concentration in the range delimited by the intermediate quantities $\tilde{C}_{p,I}^{n+1}$ and $\tilde{C}_{p,I+1}^{n+1}$ (which are provided by the scheme of Fig. 3). Figure 5 gives a graphical interpretation of what Eqs. 27 and 28 do and show why this algorithm prevents the apparition of large oscillations. This version of the explicit Euler-Lagrange method has several advantages. First, it is accu-

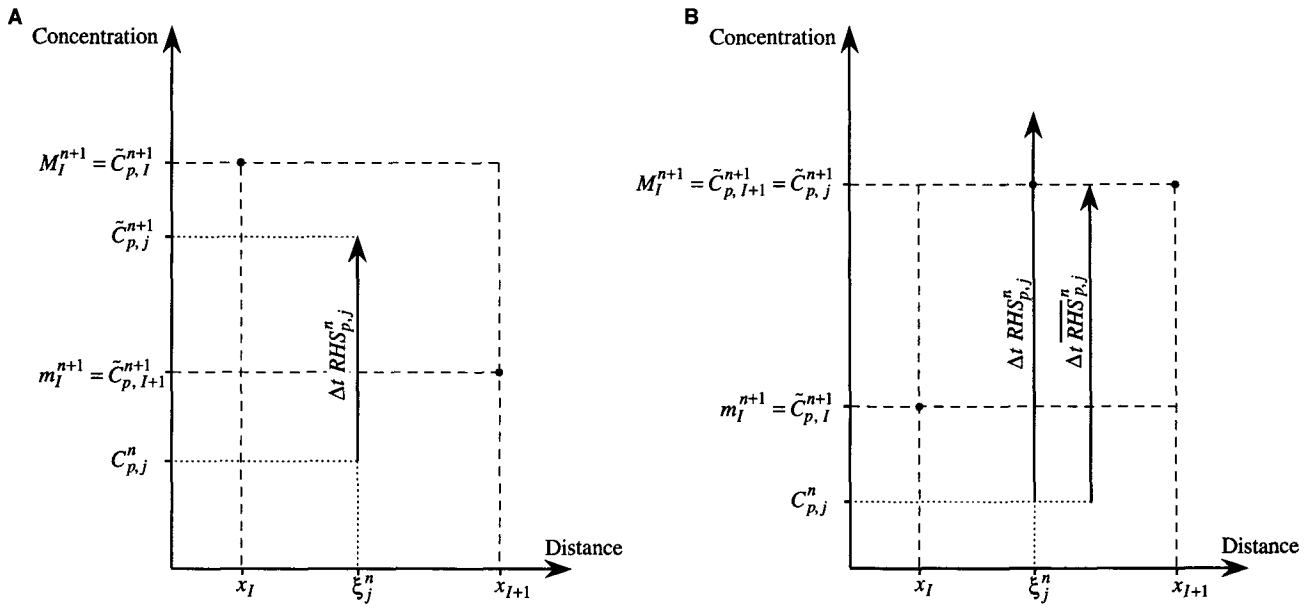

FIGURE 5. Rationale for the algorithm of Eqs. 27 and 28. The goal is to keep the provisional value of the plasma concentration on the j mesh $\tilde{C}_{p,j}^{n+1}$ between the intermediate quantities $\tilde{C}_{p,I}^{n+1}$ and $\tilde{C}_{p,I+1}^{n+1}$. (A) When $\Delta t\ \mathrm{RHS}_{p,j}^n$ is added to $C_{p,j}^n$, the result is in the range $[m_I^{n+1}; M_I^{n+1}]$, so $\overline{\mathrm{RHS}}_{p,j}^n = \mathrm{RHS}_{p,j}^n$. (B) In this example, $(C_{p,j}^n + \Delta t\ \mathrm{RHS}_{p,j}^n)$ falls outside of $[m_I^{n+1}; M_I^{n+1}]$. Therefore, Eq. 28 limits the amount added to $C_{p,j}^n$ to $\Delta t\ \overline{\mathrm{RHS}}_{p,j}^n$, which is chosen such that $\tilde{C}_{p,j}^{n+1} = M_I^{n+1}$. Notice that on both diagrams, the effect of the convection step is not shown.

rate even in the presence of steep concentration gradients. Next, its computational cost is half that of previous schemes. Finally, the stability analysis performed in the previous section directly applies to this algorithm.

MacCormack Method and Flux-Corrected MacCormack Method

The MacCormack method (21) is a finite difference method that uses a predictor step followed by a corrector step to achieve second-order accuracy in both space and time. Its application to a linear chromatography problem is derived by Finlayson (pp. 324–325 of Ref. 12). To extend the method to the nonlinear BTEX model, it is necessary to replace the transport and reaction rate constants of the linear model by the concentration-dependent permeabilities and reaction rates. Thus, the predictor step is applied with PS's and G's evaluated with the current concentrations, whereas in the corrector step, PS's and G's are estimated with the predicted concentrations.

As described by Finlayson (12), the flux-corrected transport algorithm of Boris and Book (6) can be added to the MacCormack method to cure oscillations that appear when a steep concentration front is present in the plasma. When the solution does not have discontinuities or sharp axial gradients, the flux correction serves only to increase the computational cost at no gain in accuracy. Transport in the microcirculatory system seems to exhibit enough dispersion to eradicate steep axial gradients, so that the flux-corrected transport algorithm is not used. The most reliable "sharp front" indicator is the appearance of oscillations in the solution from node to node. "Excessive dispersion" occurs for low Peclet number, in the range of 1 to 10.

In opposition to the random choice and Euler-Lagrange techniques, the MacCormack method is conservative (18). The implication in BTEX modeling is that, for a substrate that is not consumed, the mass that flows out of the exchange unit and is estimated with the computed solution is equal to the mass of substrate injected:

$$q_{\text{out}} \approx F_p \, \Delta t \sum_{n=0}^{\infty} C_{p,N_{\text{seg}}}^{n} = F_p \, \Delta t \sum_{n=0}^{\infty} C_{p,0}^{n} \approx q_{in}.$$

This equality remains true even when the error in the numerical approximation of C_p is significant. Whether it is advantageous or not for the numerical technique to have a conservative property is an issue to which many differing answers have been given (see pp. 32–33 of Ref. 27). As far as BTEX modeling is concerned, we have not observed any important benefit of using a method conserving mass. The nonconservative character of the random choice and Euler-Lagrange techniques proves actually more useful, because mass conservation checks provide quick insights on the accuracy of the numerical solution.

RESULTS AND DISCUSSION

Accuracy and Efficiency of the Numerical Techniques

Before the present model is used to analyze actual experiments, it is important to check its correctness by applying it to simple problems with known solutions. For instance, let us reduce Eqs. 1 and 2 to

$$\frac{\partial C_p}{\partial t} + \frac{F_p L}{V_p} \frac{\partial C_p}{\partial x} = - \frac{\mathrm{V}_{\max_p}}{V_p(\mathrm{K}_{\mathrm{m}_p} + C_p)} C_p. \qquad (29)$$

This is done by choosing an enzymatic reaction process in the plasma and by shutting down barrier transport and axial diffusion. The solution to this simple model is expressed in terms of the reference concentration (8), although the concentration is expressed implicitly and must be solved for numerically; Linehan and coworkers (10,20) have used it extensively to study the unidirectional, saturable uptake of various substrates in the lung. For our purpose, the exact solution of Eq. 29 provides a reference against which numerical approximations can be checked. A comparison between the MacCormack solution and the pseudoanalytical solution is displayed in Fig. 6. Figures 6b,c use different scales to show the tracer concentration-time curve at the outlet of the BTEX unit after the injection of a bolus containing q_{tot} moles of labeled and unlabeled substrate. In this simulation, the amount of tracer is proportional to that of mother substance; so, concentrations shown in Fig. 6 are divided by q_{tot} for scaling purposes. The variations of the extraction ratio for the same computation are displayed in Fig. 6a. When the value of q_{tot} is low, the system is linear. In such case, the substrate is removed at a constant rate, and the instantaneous extraction remains constant. As the total amount of substrate is increased, however, nonlinearities appear as is shown by the dip in the extraction curve. The decrease in the extraction reflects the saturation of the consumption process. The diminishment of the area confined between the normalized concentration curves for reference and tracer is also characteristic of this saturation. The particular model parameters used in this simulation are given in the caption of the figure. Notice that, although parameters are chosen in a range that corresponds to physiological conditions, no particular importance is attached to their values because, for now, our goal is simply to verify the correctness of the model output. Figure 6 demonstrates that the agreement between MacCormack, and exact solutions are very good when the model is approximating a simple limiting case whose behavior is nonlinear. For the same test problem,

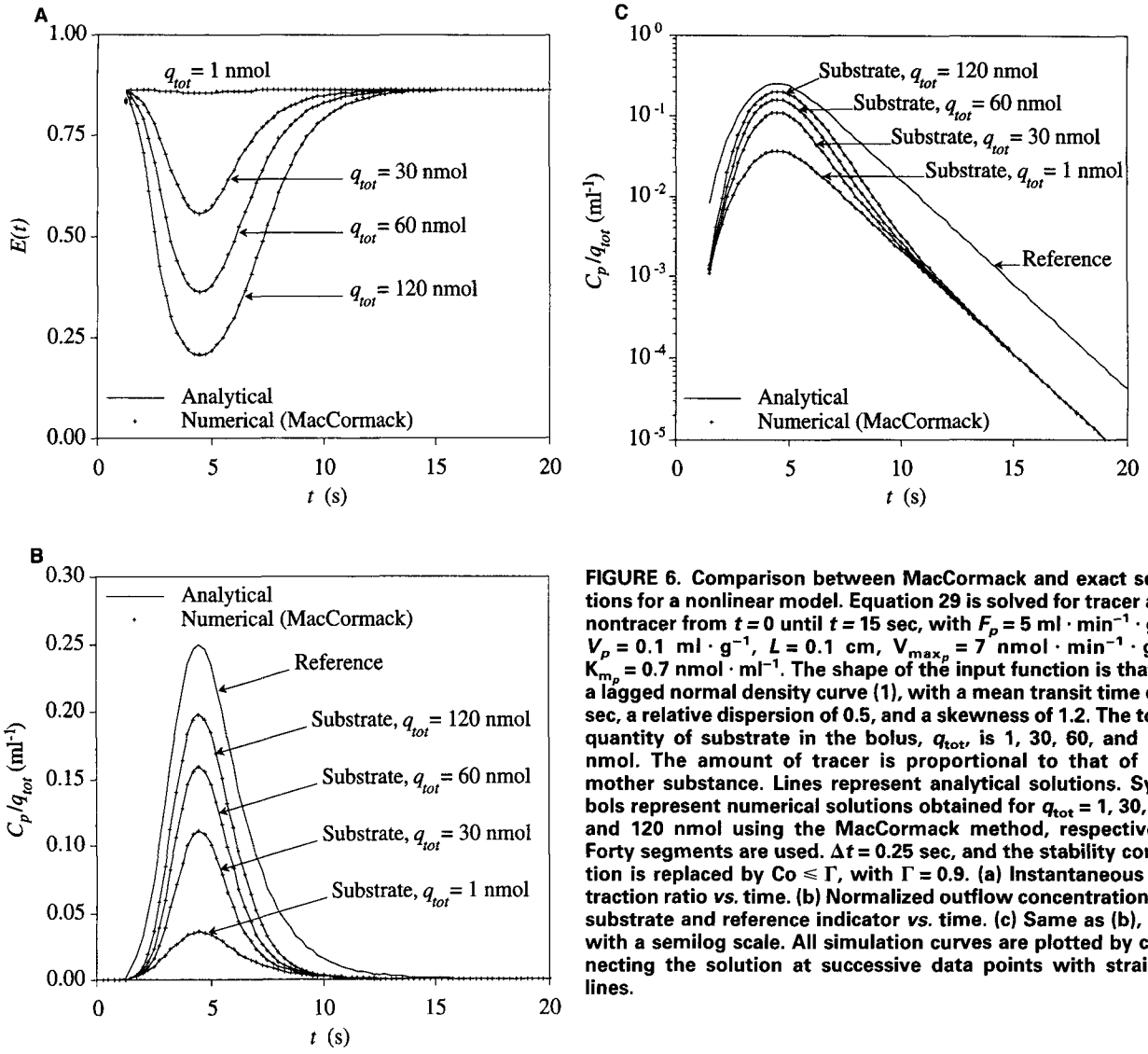

FIGURE 6. Comparison between MacCormack and exact solutions for a nonlinear model. Equation 29 is solved for tracer and nontracer from $t = 0$ until $t = 15$ sec, with $F_p = 5$ ml · min^{-1} · g^{-1}, $V_p = 0.1$ ml · g^{-1}, $L = 0.1$ cm, $V_{max_p} = 7$ nmol · min^{-1} · g^{-1}, $K_{m_p} = 0.7$ nmol · ml^{-1}. The shape of the input function is that of a lagged normal density curve (1), with a mean transit time of 4 sec, a relative dispersion of 0.5, and a skewness of 1.2. The total quantity of substrate in the bolus, q_{tot}, is 1, 30, 60, and 120 nmol. The amount of tracer is proportional to that of the mother substance. Lines represent analytical solutions. Symbols represent numerical solutions obtained for q_{tot} = 1, 30, 60, and 120 nmol using the MacCormack method, respectively. Forty segments are used. $\Delta t = 0.25$ sec, and the stability condition is replaced by Co $\leq \Gamma$, with $\Gamma = 0.9$. (a) Instantaneous extraction ratio *vs.* time. (b) Normalized outflow concentration for substrate and reference indicator *vs.* time. (c) Same as (b), but with a semilog scale. All simulation curves are plotted by connecting the solution at successive data points with straight lines.

the Euler-Lagrange technique and random choice method also yield very good results that are not displayed herein. However, both of these techniques require more nodes in the linear range than needed by the MacCormack method to provide a solution that looks as good. If the problem is nonlinear, the Euler-Lagrange and random choice methods provide solutions just as good as the MacCormack method with the same number of nodes.

In Fig. 7, the accuracy and the efficiency of each numerical method are studied more precisely. Equation 29 is solved for C_p, the nontracer concentration, with a set of parameters and inputs (given in the caption of the figure) such that conditions in the system are nonlinear. For each numerical technique, a solution is computed with an initial number of segments equal to 20, 40, 80 and 160. In all cases, the Courant number is one half. Because methods that work for Co = 1 sometimes do not work for Co $\neq$ 1, it is important to test a method with Co $\neq$ 1. For each trial, the L_2-norm of the error with respect to the exact solution is plotted *versus* the computational time obtained on a Sun SPARCserver 470.

$$\text{Error} = \left\{ \frac{1}{T} \int_0^T [C_{p,\text{out}}(t) - C_{p,\text{out}}^{\text{exact}}(t)]^2 \, dt \right\}^{1/2}.$$

Even though the test case is simpler than Eqs. 1 and 2, the times shown are those it takes to compute the full two-region model with tracer and nontracer substrates, because reduction to the test equation is achieved by setting relevant parameters to zero. As expected, each numerical technique has less error as the number of segments increases, and the computational cost increases as the accuracy improves. Similar trends are observed when the error is estimated with the L_1 or the L_∞ norm. The random choice and Euler-Lagrange schemes are very close to each other. For a given number of segments, they produce so-

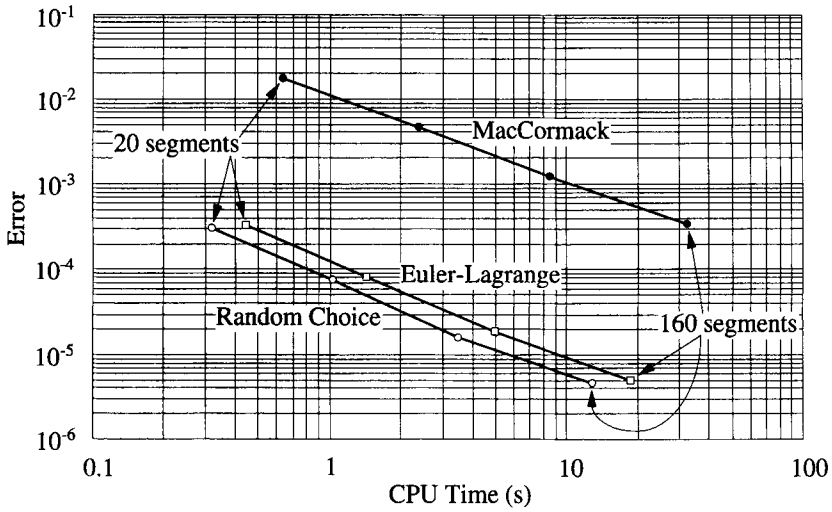

FIGURE 7. Efficiency plot. Equations 1 and 2 are solved for C_p from $t = 0$ until $t = 20$ sec, with $F_p = 6$ ml · min^{-1} · g^{-1}, $V_p = 0.1$ ml · g^{-1}, $L = 0.1$ cm, $V_{max_p} = 30$ nmol · min^{-1} · g^{-1}, $K_{max_p} = 4$ nmol · ml^{-1}, $T_T = 0$ mol · g^{-1}, and $D_p = 0$ cm^2 · sec^{-1}. The input function is a Gaussian curve, with a mean of 6 sec and a relative dispersion of 0.5. The total quantity of substrate in the bolus is 50 nmol. Numerical solutions are computed for an initial number of segments equal to 20 (leftmost symbols), 40, 80, and 160 (rightmost symbols). In each case, the L_2 norm of the error with respect to the exact solution is plotted *versus* the computational time. For each simulation, the Courant number is fixed to 0.5.

lutions with approximately the same error. Nevertheless, the random choice method is slightly faster than the moving grid technique. This difference reflects the cost of interpolating from the moving mesh to the fixed grid and vice-versa. The MacCormack method is obviously less efficient for this test case. It is about twice as slow as the other methods, and its slowness is not offset by better accuracy. However, these results must be contrasted. First, let us remark that even the MacCormack method is an accurate method because, for the problem of Fig. 7, the computed concentration at the peak of the outflow curve remains within 0.6% of the exact solution. Such accuracy is often sufficient in the analysis of experimental data wherein many other uncertainties exist. Moreover, when the test of Fig. 7 is conducted with a Courant number equal to 1, the efficiency of the MacCormack method becomes comparable with that of the other techniques.

The main drawback of the MacCormack method comes from the difficulty of deriving a practical stability criterion. The Von Neumann stability analysis is more complicated for the MacCormack method because convection, reaction, transport, and diffusion are all treated simultaneously. Therefore, it is not possible to derive analytically a stability criterion. The MacCormack method also requires two evaluations of the *PS*'s and *G*'s per time step. As a result, the MacCormack method is not as well suited as the random choice and Euler-Lagrange techniques to meet our requirements of speed, accuracy, and robustness.

This example should remind us of the difficulty of comparing numerical methods. To compute the efficiency of a technique, one must know computational cost and error. Although the former is fairly predictable, the behavior of the latter is more uncertain. This stems from the fact that results produced by a numerical technique are affected by several types of error (truncation error and round-off error). Unfortunately, the behavior of each of these components is not completely predictable, and it is therefore difficult to know in advance what the resultant of the error will be in a particular situation. Therefore, the best method for one problem is not necessarily the best method for another problem. In this context, our strategy is to present investigators with several numerical techniques. Then, one has the ability to check that results of one method corroborate results of the other.

To illustrate this point further, we show a comparison of the three numerical methods applied to a stiff nonlinear problems for which an analytical solution does not exist. Equations 1 and 2 with all reaction and axial diffusion terms set to zero are solved for the conditions shown in the caption of Fig. 8. Notice that $p_{+0} = p_{-0} = p_{+1} = p_{-1} = p$, so that $T_T$and p are not independent parameters. Thus, it is sufficient to specify $T_T p/2$. The problem is stiff (and therefore difficult to solve numerically) because the dimensionless ratio *PS/F* is high. It ranges from about 100 to 600. Figures 8a,b compare the MacCormack and random choice solutions, whereas Figs. 8c,d compare the MacCormack and Euler-Lagrange solutions. The plasma outflow concentration-time curves provided by the three techniques are in close agreement. The extraction curves slightly disagree because the calculation of the extraction amplifies small differences that were not detectable with the concentration curves. The random choice extraction-time curve is jagged because this numerical method does not propagate the solution wave smoothly in the spatial dimension, but by fixed increment of size Δx. Like the random choice method, the Euler-Lagrange technique sometimes produces jagged solutions. This is caused by the limiter of Eqs. 27 and 28 that ensures that large oscillations will not develop when the time step is too big, but works in such a way that the Euler-Lagrange solution for C_p might slightly vary around the true solution. As in the random choice method, these subtle variations are usually not problematic, unless they are largely amplified as is the case in Fig. 8a for the random choice

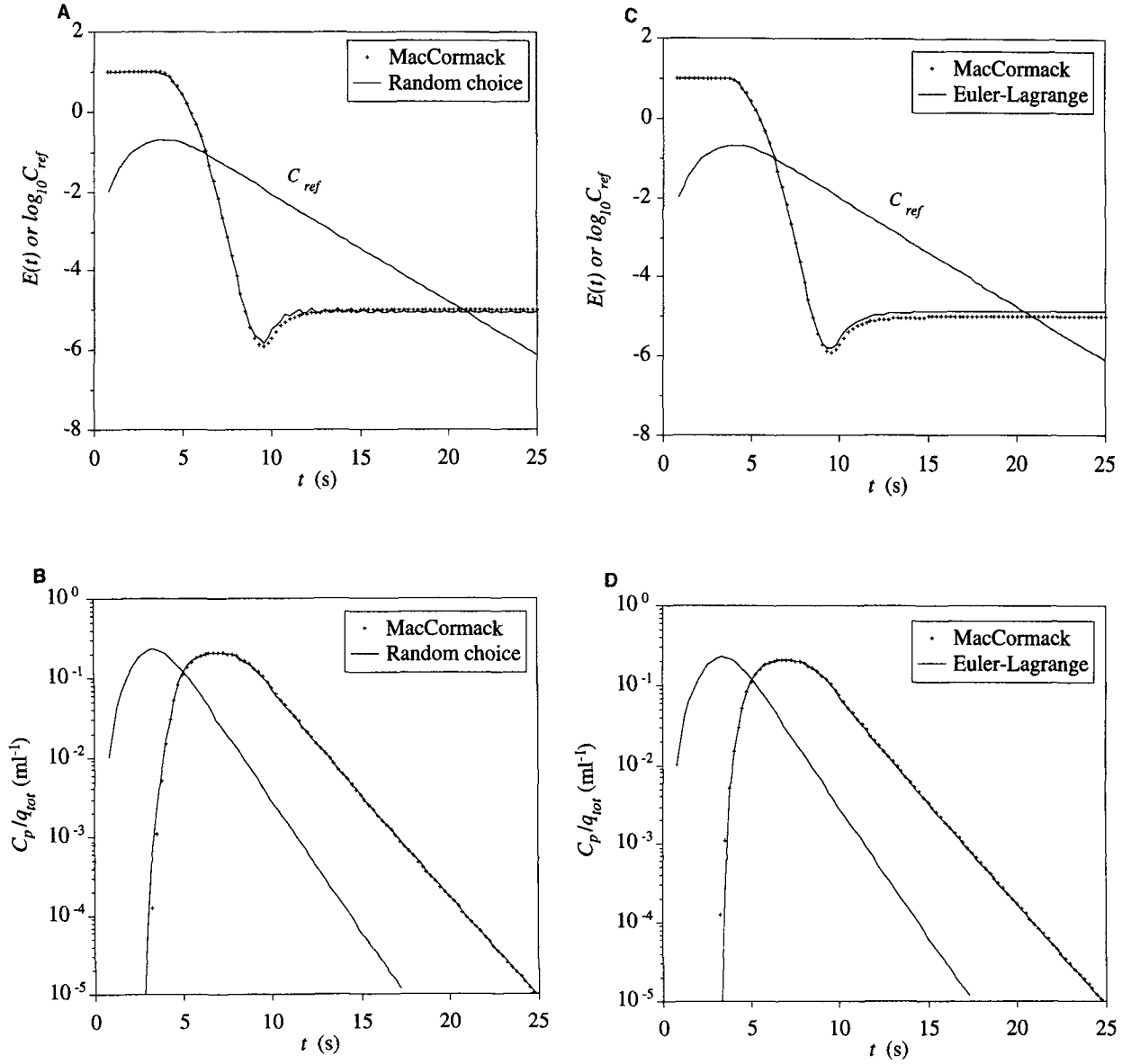

FIGURE 8. Comparison between numerical methods for a stiff, nonlinear problem with known analytical solution. Equations 1 and 2 are solved from $t = 0$ to $t = 25$ sec, with $F_p = 5$ ml · min^{-1} · g^{-1}, $V_p = 0.05$ ml · g^{-1}, $V_c = 0.25$ ml · g^{-1}, $L = 0.1$ cm, $K_{s_p} = K_{s_c} = 1$ nmol · ml^{-1}, $p_{+0} = p_{-0} = p_{+1} = p_{-1} = p$, and $pT_T/2 = 3{,}000$ nmol · min^{-1} · g^{-1}. There is no reaction and no axial diffusion. The input function is a lagged normal density curve with a mean of 4 sec, a relative dispersion of 0.5, and a skewness of 1.2. The total quantity of substrate in the bolus is 120 nmol. Euler-Lagrange and random choice solutions are obtained with 100 initial segments and $\Gamma = 0.8$. The MacCormack method is applied with 75 segments and Co ≤ 0.15. (a and c) The instantaneous extraction as a function of time. (b and d) The plasma concentration at the capillary outlet divided by the total mass of substrate injected as a function of time. MacCormack (symbol) and random choice (line) solutions are compared in (a) and (b). MacCormack (symbol) and Euler-Lagrange (line) solutions are compared in (c) and (d). The random choice method is the fastest; the Euler-Lagrange technique and MacCormack method are 1.2 and 2.1 times slower, respectively.

method. The concentration curves plotted *versus* distance at one time are not jagged.

Random Choice, Euler-Lagrange, and Sliding Fluid Methods

The random choice and the Euler-Lagrange techniques resemble the sliding fluid element model with finite difference formulation of Bassingthwaighte *et al.* (3). In fact, all three methods treat convection separately from the rest of the physical processes and use finite differencing to integrate the resulting system of ordinary differential equations. Each method, however, has its own way of solving the convection step, even though there is no apparent distinction when the Courant number is unity. In addition, the three techniques do not integrate Eq. 11 in the

same manner. For linear models without axial diffusion, Bassingthwaighte *et al.* use the fact that

$$\mathbf{C}^{n+1} = e^{\mathbf{A}\Delta t}\mathbf{C}^n, \tag{30}$$

and approximate the exponential term with high-order Padé or Taylor series approximations to derive a finite difference expression. Because these high-order schemes yield very good results (4), one could wonder whether they can also be applied with the random choice or Euler-Lagrange techniques. The answer is yes. However, the resulting high-order schemes work well only for linear problems and, therefore, are not described in the present paper, which is concerned with nonlinear applications. To illustrate the difference between linear and nonlinear problems (in Fig. 9a), Taylor series of $o(\Delta t^2)$ and $o(\Delta t^3)$ are used to approximate $e^{\mathbf{A}\Delta t}$ in Eq. 30. These approximations are used to create two forms of the random choice method. The first uses a Taylor series of $o(\Delta t^2)$ and corresponds exactly to the random choice method described earlier. The second uses a Taylor series of $o(\Delta t^3)$. When these two forms of the random choice method are used to solve a linear problem, Fig. 9a shows that the scheme using a Taylor series of $o(\Delta t^3)$ is more accurate by 4 orders of magnitude. Because it does not require many additional floating point operations, it is also more efficient. These conclusions, however, do not necessarily hold when a nonlinear problem is solved. Figure 9b shows an example where the higher order scheme is the less efficient. This behavior arises because for nonlinear problems the derivation of Eq. 30 is not exact. Therefore, expanding $e^{\mathbf{A}\Delta t}$ with more terms in the Taylor series does not yield better results. To perform the time integration more accurately, it is in fact necessary to apply high-order schemes designed for nonlinear problems (11). For each new method, however, the trade-off between accuracy, speed, and memory requirements needs to be evaluated. A robust package also requires a strategy to adjust the time step. In the remainder of this study, we will only use the random choice and Euler-Lagrange techniques in conjunction with a Taylor series of $o(\Delta t^2)$ to approximate $e^{\mathbf{A}\Delta t}$ (*i.e.*, with the explicit first-order Euler scheme to integrate in time).

Modeling "Backdiffusion," Return Flux from Tissue to Blood

We mentioned earlier that Eq. 29 has been used to model the saturable uptake of various substrates in the lung. This model is appropriate under the assumptions of homogeneous organ perfusion and negligible backdiffusion. Backdiffusion is defined as the reflux into the plasma of substrate that has been previously absorbed. In the next section, we show how the BTEX unit introduced in this study alleviates the requirement for unidirectional mass exchange in the analysis of experimental data. Linehan *et al.* (20) solved a similar model (without axial dispersion or

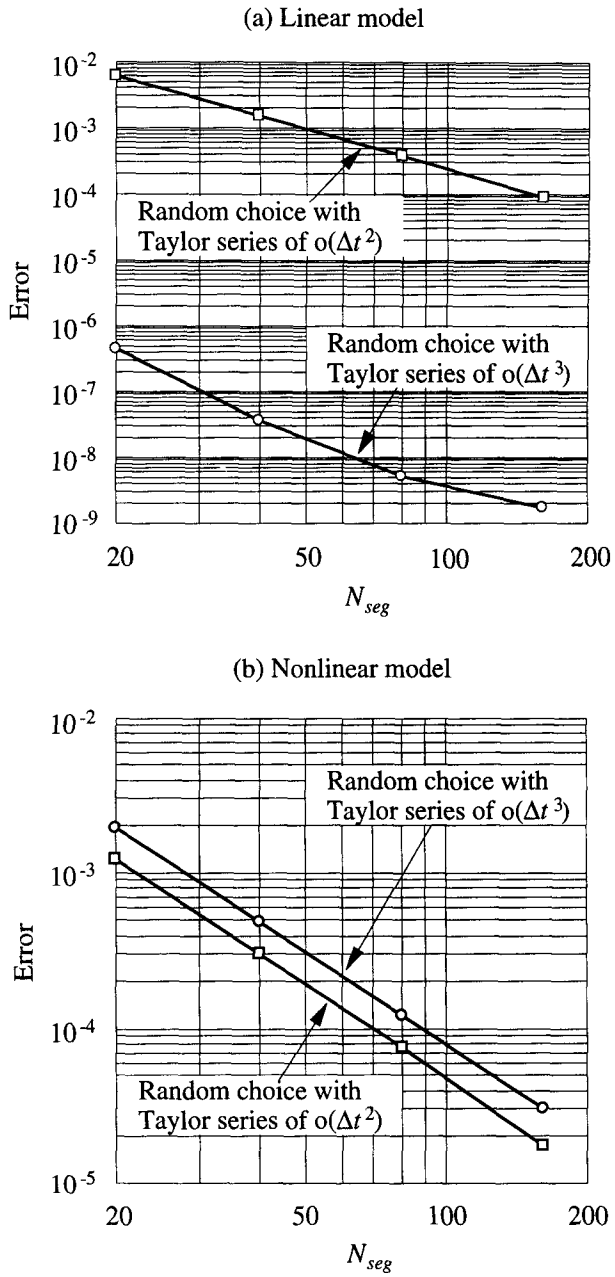

FIGURE 9. Numerical error in the L_2 norm *versus* number of segments when two forms of the random choice method that use a Taylor series of $o(\Delta t^2)$ and of $o(\Delta t^3)$, respectively, to approximate $e^{\mathbf{A}\Delta t}$ are applied to a linear and a nonlinear problem. (a) Linear problem: Eq. 28 with the right-hand side replaced by $(-G_{max_p} C_p/V_p)$ is solved with $F_p = 6$ ml · min^{-1} · g^{-1}, $V_p = 0.1$ ml · g^{-1}, $L = 0.1$ cm, $G_{max_p} = 3$ nmol · min^{-1} · g^{-1}. The shape of the input function is given by a lagged normal density curve with a mean of 4 sec, a relative dispersion of 0.5, and a skewness of 1.2. The total quantity of substrate in the bolus is 5 nmol · g^{-1}. (b) Nonlinear problem: Eq. 28 is solved with $V_{max_p} = 30$ nmol · min^{-1} · g^{-1}, $K_{max_p} = 4$ nmol · ml^{-1}. All other parameters are as in (a). For both figures, the Courant number is unity.

reaction), but they do not describe the mathematical method used.

Instead of simulating the removal of substrate with a reaction term like Eq. 29, let us use the transporter with $p_{+0} = p_{-0} = p_{+1} = p_{-1} = p$. Then, the permeability-surface area products become:

$$PS_{p\to c} = \frac{T_T p}{2}\frac{1}{K_{s_p} + C_p} \quad \text{and} \quad PS_{c\to p} = \frac{T_T p}{2}\frac{1}{K_{s_c} + C_c}. \tag{31}$$

When, in addition, the equilibrium constant K_{s_c} is large with respect to C_c and $C_c(T_T p/2)$, the aforementioned equation shows that the flux from tissue to plasma is small and linear, so that there is little backdiffusion. Figure 10 illustrates the model behavior when the binding equilibrium constant at the barrier–tissue interface spans a wide range of values. Figure 10a shows the changing shape of the extraction curve as the ratio $\kappa = K_{s_c}/K_{s_p}$ goes from 10^5 to 10^{-2}. For the highest value, the curve resembles that of Fig. 6, because there is almost no reflux of tracer. For $\kappa = 10^4$, it is only after about 15 sec that the tail of the extraction curve bends down, indicating that tracer is diffusing back toward the plasma space. As κ is decreased, backdiffusion becomes noticeable earlier. This makes sense because then K_{s_c} becomes smaller, the retention of tracer in the tissue diminishes as well. Eventually, when κ approaches 0, the tracer is denied access to the tissue region. Therefore, the extraction remains null. The shape of the extraction curve for $\kappa = 0.1$ is particularly interesting, because it passes through an inflection point and a minimum before leveling at a negative value. This behavior is better understood by comparing the normalized outflow concentration profiles for tracer substrate and indicator reference. These curves are shown in Fig. 10b. For $\kappa = 0.1$, the tracer concentration remains below the reference concentration until both curves reach their peak. Then, as the substrate that had accumulated in the tissue is driven back into the plasma, the tracer concentration overtakes the reference concentration. This difference grows until a time of about 8 sec and finally returns to levels about 20% higher than the reference tracer concentration as the remaining substrate is washed out of the capillary unit. Notice that, in Figure 10b, the profile for $\kappa = 0.01$ is not graphed, because it is not distinguishable from the reference curve.

Although the shape of the extraction ratio curve provides good indication on the importance of backdiffusion, it only gives information for the limited period of time when the reference concentration is not 0. In contrast, when backdiffusion is present but not too important, the tracer concentration curves can remain visible for a long period of time. Figure 11 shows the tail of the tracer concentration curve for several values of κ. For $\kappa \geq 1$, for

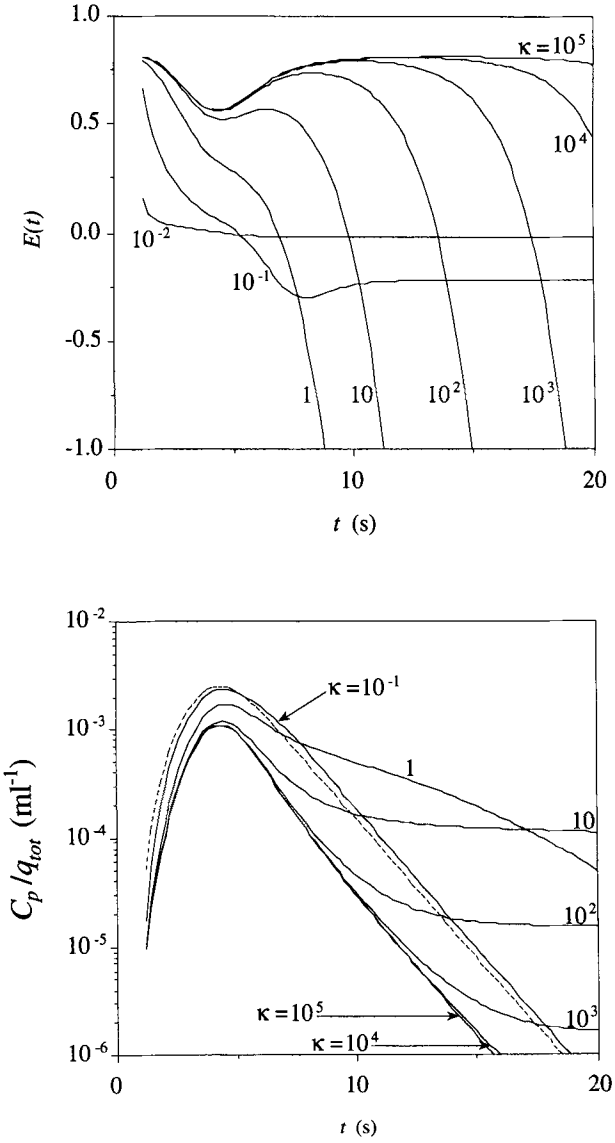

FIGURE 10. Effect of backdiffusion on the shape of the instantaneous extraction ratio and of the outflow concentration curves at short times. A bolus containing reference indicator and tracer and nontracer substrate is injected into the BTEX unit for which: $F_p = 3$ ml · g^{-1} · min^{-1}; $V_p = 0.05$ ml · g^{-1}; $V_c = 0.15$ ml · g^{-1}; $L = 0.1$ cm; no reaction; no axial diffusion; $p_{+0} = p_{-0} = p_{+1} = p_{-1} = 0.6$ min^{-1}; $T_T = 16.667$ nmol · g^{-1}, $K_{s_p} = 1$ nmol · ml^{-1}, and $K_{s_c} = \kappa K_{s_p}$. The shape of the input function is given by a lagged normal density curve with a mean of 4 sec, a relative dispersion of 0.5, and a skewness of 1.2. The total quantity of substrate in the bolus is 30 nmol. (a) Extraction ratio *versus* time. (b) Normalized outflow concentration *versus* time. The dotted line represent the reference indicator. For clarity, the substrate concentration profile for $\kappa = 0.01$ is not shown, because it falls on the reference curve.

example, it is clear that the tail carries information about the exchange process. Consequently, the interpretation of experimental data requires that observation be made long enough. Of course, it might not be easy to determine *a priori* to what extent measurements are needed, but one might gain valuable insight by using the predictive nature

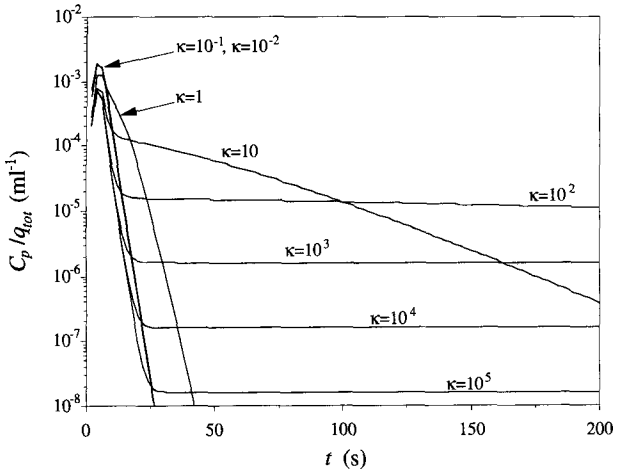

FIGURE 11. Effect of backdiffusion on the shape of the outflow concentration curves at long times. Conditions are identical to those of Fig. 10, but the solution is computed until $t = 200$ sec. In addition, a semilogarithmic scale is used for plotting. For moderate to high values of κ, the tail of the concentration curve provides information on the rate of backdiffusion. However, when κ is very small (κ < 0.1), long time solutions do not provide additional information.

of the computer model early in the design stage of the experimental procedure. Although measurements can be made over several orders of magnitude, Fig. 11 is calculated over 6 orders of magnitude to show the trends with κ.

Steady-State Plasma-Tissue Concentration Gradients

One of the peculiarities of the transporter model is that permeability-surface area products from plasma to cells and from cells to plasma need not be equal. It is easy to show that this asymmetry can lead to the formation of a steady-state concentration difference between plasma and intracellular regions even in the absence of consumption. When there is only radial exchange and convective transport, the fluxes $PS_{p\rightarrow c}C_p$ and $PS_{c\rightarrow p}C_c$ are equal at steady-state. From this equality, one readily derives:

$$\frac{C_p}{C_c} = \frac{p_{-1}\, p_{+0}\, K_{s_p}}{p_{+1}\, p_{-0}\, K_{s_c}}. \tag{32}$$

This shows that there are many possibilities under which a steady-state concentration gradient can develop. For the situation we used to model backdiffusion, for example, all of the permeabilities for free-transporter and transporter-substrate complex are equal. As a result, the steady-state concentration difference is determined by the ratio of the binding equilibrium constants. The substrate accumulates preferentially in the intracellular region when $K_{s_c} > K_{s_p}$, in the plasma region when $K_{s_p} > K_{s_c}$, and there is no asymmetry when the equilibrium constants are equal. Of course, it is also possible that no steady-state gradient will exist when $K_{s_p} \neq K_{s_c}$, but this can only occur when some asymmetry among the permeabilities for free transporter and complex exists.

Modeling Axial Diffusion

The present BTEX model allows inclusion of axial diffusion, which is modeled with a diffusion term as shown in Eq. 1. Inspection of Eq. 20 shows that terms due to the presence of axial diffusion impose a restriction on the time step that is proportional to $\Delta x^2/D$. Thus, doubling the number of segments on the spatial mesh necessitates the use of a time step 4 times smaller. One should keep this limitation in mind and appropriately reduce the number of mesh points when axial diffusion coefficients become large in order not to compromise computational efficiency.

Not surprisingly, the effects of axial diffusion on the nonlinear model are similar to those described by Bassingthwaighte *et al.* (3,4) for linear models. In the tissue, the spreading effect of diffusion flattens concentration profiles along the length of the capillary. This, in turn, influences the rate at which tracer returns to the plasma in the stages after passage of the bolus. In the plasma, however, the effect of axial diffusion is more important during the initial rise of the concentration. In addition, the shape of the concentration curve is less affected than that of the instantaneous extraction ratio. The latter is most sensitive to the difference between the diffusion coefficient for substrate, D_p^{sub}, and that for the reference indicator, D_p^{ref}. This behavior is expected because, by definition, the instantaneous extraction includes the substrate to reference normalized concentration ratio. The influence of axial diffusion on the instantaneous extraction is also important when $D_p^{\text{sub}} = D_p^{\text{ref}}$. An example is displayed in Fig. 12. Herein, the situation is identical to that of Fig. 6, but axial diffusion coefficients for reference and substrate have been set to 10^{-3} cm$^2 \cdot$ sec^{-1}. As the bolus enters the capillary, the instantaneous extraction is diminished. This decrease becomes more pronounced as D_p increases. When the total quantity of substrate in the bolus is sufficiently low, the extraction rises until it levels off. For higher doses, the minimum in the extraction curve is still present, but it no longer occurs simultaneously with the peak of the concentration curves. Later, in time, the extraction returns to a constant value that is slightly below that observed in the absence of axial diffusion. The value of D_p used in Fig. 12 might be high in comparison with actual diffusion coefficients, but this choice is deliberate. In fact, a large diffusion coefficient gives a clearer graph by amplifying the phenomena observed for lower D_p. Most importantly, we have chosen this value because it provides a picture that is remarkably similar to Fig. 5 of Ref. 18. To obtain this figure, Linehan and his coworkers used Eq. 29 to represent the uptake of substrate in a capillary, but built a

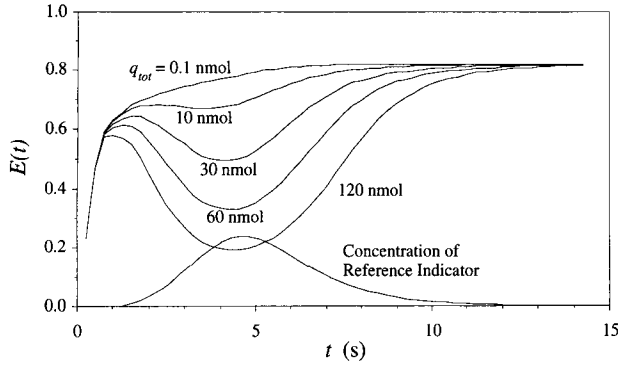

FIGURE 12. An example of the effect of axial diffusion on the instantaneous extraction. A bolus containing a reference indicator and a known dose of substrate is injected in a single BTEX unit such that: $F_p = 5$ ml · g^{-1} · min^{-1}; $V_p = 0.1$ ml · g^{-1}; $L = 0.1$ cm; there is no radial transport ($T_T = 0$); reaction in plasma follows Michaelis-Menten kinetics with $V_{max_p} = 7$ nmol · min^{-1} · g^{-1} and $K_{m_p} = 0.7$ nmol · ml^{-1}, and $D_p = 10^{-3}$ cm^2 · sec^{-1}. The coefficient of axial diffusion is the same for intravascular reference and substrate. The shape of the input function is given by a lagged normal density curve with a mean of 4 sec, a relative dispersion of 0.5, and a skewness of 1.2. The total quantity of substrate in the bolus is successively 0.1, 10, 30, 60, and 120 nmol.

model (including several capillaries placed in parallel and with different transit times) to simulate heterogeneities within a lung. In contrast, we have used a single capillary for the entire organ. This is similar to the Turner capacitance model described by Rowlett and Harris (28). The resemblance between Linehan's Fig. 5 and our Fig. 12 illustrates that axial diffusion and flow heterogeneities have similar effects, because both introduce dispersion in the system. By doing experiments at different flow rates, the two phenomena might be differentiated. The effect of axial dispersion would be reduced as the flow rate was increased, whereas the dispersion due to different transit times would remain the same as the flow rate was increased.

Parameter Estimation

The chief issue in parameter estimation is whether parameters can be estimated accurately given experimental data. Bassingthwaighte *et al.* (4) have shown that linear BTEX models combined with a nonlinear curve-fitting program called SENSOP (9) give good parameter estimates. As one would expect, the quality of the estimates depends heavily on the availability of good data (*i.e.*, data with little noise and good time resolution). In the next section, we present parameter estimation results for the nonlinear model.

For testing Eq. 29, we look for the estimates of V_{max_p} and K_{m_p} given 21 data points collected every 0.25 sec from $t = 3.75$ until $t = 9.00$ sec. The initial guesses are $V_{max_p} = 7.5$ and $K_{m_p} = 0.4$. Data are obtained from the analytical solution to the model equation when $F_p = 2$ ml · g^{-1} · sec^{-1}, $V_p = 0.05$ ml · g^{-1}, $L = 0.1$ cm, $V_{max_p} = 5$ nmol · g^{-1} · min^{-1}, and $K_{m_p} = 0.5$ nmol · ml^{-1}. In addition, the input function is given by a lagged normal density curve with a mean transit time of 5 sec, a relative dispersion of 0.4, a skewness of 1.2, and such that the total quantity of substrate in the bolus is 1 nmol · g^{-1}. The problem is solved using the random choice method, and the parameters are changed using the nonlinear optimizer SENSOP to pick the best values of V_{max_p} and K_{m_p}. The estimates are shown in the left-hand column of Table 1. When the number of segments is above 20, it is seen that parameter estimates converge to the exact parameter values, because the absolute error is roughly divided by two when the number of segments is multiplied by the same factor. With fewer segments (*i.e.*, 5 and 10), the convergence trend is not apparent because the numerical solution lies too far away from the exact solution. Such a situation usually leads to bad parameter estimates, but can often be detected by visual inspection of the solution. The same calculation, but using the Euler-Lagrange method to solve the problem, gives the results shown in the right-hand column of Table 1.

In a second experiment, 5% random Gaussian noise is added to the noise-free data. Table 2 displays the average of the estimates obtained after repeating the optimization for 20 noisy datasets. In this case, parameters are computed with SENSOP used in combination with the Euler-Lagrange technique and the analytical solution, for comparison. As in the example without noise, the optimizer and the numerical technique (*i.e.*, the Euler-Lagrange method herein), provide convergent parameter estimates once enough grid points are used (above 10 segments herein). However, they do not converge toward the exact solution of $V_{max_p} = 5$ nmol · g^{-1} · min^{-1} and $K_{m_p} = 0.5$ nmol · ml^{-1}. Instead, they seem to converge toward the estimates provided by SENSOP and the analytical solution for the same sets of noisy data.

In conclusion, efficient estimation of parameters from real data requires using enough grid points to obtain reasonable estimates, but not too many to keep the computational cost down, and the parameter estimation can be done for the nonlinear model (Eq. 29).

TABLE 1. Parameter estimation versus number of segments.

	Random choice		Euler-Lagrange	
N_{seg}	V_{max_p}	K_{m_p}	V_{max_p}	K_{m_p}
5	5.736	0.861	4.906	0.455
10	5.086	0.491	5.019	0.528
20	5.012	0.518	5.011	0.517
40	5.007	0.510	5.007	0.510
80	5.003	0.505	5.003	0.505
160	5.001	0.502	5.001	0.502
Exact	5.000	0.500	5.000	0.500

TABLE 2. Parameter estimation in the presence of 5% random Gaussian noise added to a noise-free known solution

N_{seg}	V_{max_p} (Mean ± SD)	K_{m_p} (Mean ± SD)
5	4.901 ± 0.067	0.446 ± 0.063
10	5.011 ± 0.070	0.518 ± 0.067
20	5.004 ± 0.069	0.508 ± 0.066
40	4.999 ± 0.069	0.500 ± 0.065
80	4.995 ± 0.069	0.494 ± 0.064
Analytical	4.992 ± 0.069	0.490 ± 0.064

For 20 noisy datasets, parameters are estimated with SENSOP plus the Euler-Lagrange method for different value of the initial number of segments, and with SENSOP plus an analytical model solution (last row).

CONCLUSION

We have developed a nonlinear BTEX model that includes facilitated transport, consumption, and axial diffusion. Three numerical techniques suited to nonlinear convection-dominated problems have been implemented to solve the resulting set of nonlinear partial differential equations. The random choice and the Euler-Lagrange techniques are preferred over the MacCormack method because they provide both efficiency and robustness. We have also illustrated some of the model behaviors, and have shown that the nonlinear BTEX model can provide reliable parameter estimates from noisy data. In this work, however, we have only used a single BTEX unit. This is a stringent limitation, because such a model does not allow directly for intraorgan flow heterogeneities except via the approximate method of using high degrees of intravascular axial mixing or dispersion.

REFERENCES

1. Bassingthwaighte, J. B., F. H. Ackerman, and E. H. Wood. Applications of the lagged normal density curve as a model for arterial dilution curves. *Circ. Res.* 18:398–415, 1966.
2. Bassingthwaighte, J. B., and C. A. Goresky. Modeling in the analysis of solute and water exchange in the microvasculature. In: Handbook of physiology. Section 2: The cardiovascular system. Volume IV: The microcirculation, edited by E. M. Renkin and C. C. Michel. Bethesda, MD: American Physiological Society, 1984, pp. 549–626.
3. Bassingthwaighte, J. B., C. Y. Wang, and I. S. Chan. Blood-tissue exchange via transport and transformation by capillary endothelial cells. *Circ. Res.* 65:997–1020, 1989.
4. Bassingthwaighte, J. B., I. S. Chan, and C. Y. Wang. Computationally efficient algorithms for convection-permeation-diffusion models for blood-tissue exchange. *Ann. Biomed. Eng.* 20:687–725, 1992.
5. Bird, R. B., W. E. Stewart, and E. N. Lightfoot. Transport Phenomena. New York: John Wiley and Sons, 1960.
6. Boris, J. P., and D. L. Book. Flux-corrected transport. I. SHASTA, a fluid transport algorithm that works. *J. Comp. Phys.* 11:38–69, 1973.
7. Briggs, G. E., and J. B. S. Haldane. A note on the kinetics of enzyme action. *Biochem J.* 19:338–339, 1925.
8. Bronikowski, T. A., C. A., Dawson, J. H. Linehan, and D. A. Rickaby. A mathematical model of indicator extraction by the pulmonary endothelium via saturation kinetics. *Math. Biosci.* 61:237–266, 1982.
9. Chan, I. S., A. A. Goldstein, and J. B. Bassingthwaighte. SENSOP: a derivative free solver for nonlinear least squares with sensitivity scaling. *Ann. Biomed. Eng.* 21:621–631, 1993.
10. Dawson, C. A., J. H. Linehan, D. A. Rickaby, and T. A. Bronikowski. Kinetics of serotonin uptake in the intact lung. *Ann. Biomed. Eng.* 15:217–227, 1987.
11. Finlayson, B. A. Nonlinear Analysis in Chemical Engineering. New York: McGraw-Hill, 1980.
12. Finlayson, B. A. Numerical Methods for Problems with Moving Fronts. Seattle, WA: Ravenna Park Publishing, 1992.
13. Fletcher, C. A. J. Computational Techniques for Fluid Dynamics, vol. 1. New York: Springer-Verlag, 1988.
14. Goresky, C. A. A linear method for determining liver sinusoidal and extravascular volumes. *Am. J. Physiol.* 204:626–640, 1963.
15. Harten, A. Uniformly high order accurate essentially non-oscillatory schemes. III. *J. Comput. Phys.* 71:231–303, 1987.
16. Holt, M. Numerical Methods in Fluid Dynamics. New York: Springer-Verlag, 1984.
17. Lenhoff, A. M., and E. N. Lightfoot. Convective dispersion and interphase mass transfer. *Chem. Eng. Sci.* 41:2795–2810, 1986.
18. LeVeque, R. J. Numerical Methods for Conservation Laws. Basel: Birkhauser Verlag, 1992.
19. Linehan, J. H., C. A. Dawson, D. A. Rickaby, T. A. Bronikowski, B. N. Gillis, and B. R. Pitt. Pulmonary endothelial angiotensin-converting enzyme kinetics. In: Carrier mediated transport of solutes from blood to tissue, edited by D. L. Yudilevich and G. E. Mann. London: Longman, 1985, pp. 251–264.
20. Linehan, J. H., T. A. Bronikowski, and C. A. Dawson. Kinetics of uptake and metabolism by endothelial cell from indicator dilution data. *Ann. Biomed. Eng.* 15:201–215, 1987.
21. MacCormack, R. W. The effect of viscosity in hypervelocity impact cratering. AIAA Paper No. 69-354, New York: American Institute of Aeronautics and Astronautics, 1969.
22. Malcorps, C. M., C. A. Dawson, J. H. Linehan, T. A. Bronikowski, D. A. Rickaby, A. G. Herman, and J. A. Will. Lung serotonin uptake kinetics from indicator-dilution and constant-infusion methods. *J. Appl. Physiol. Respir. Environ. Exerc. Physiol.* 57:720–730, 1984.
23. Michaelis, L., and M. L. Menten. Die Kinetik der Invertinwirkung. *Biochem. Z.* 49:333–369, 1913.
24. Poulain, C. A., and B. A. Finlayson. A comparison of numerical methods applied to non-linear adsorption columns. Int. J. Numer. Methods Fluids 17:839–859, 1993.
25. Poulain, C. A. Efficient Numerical Methods for Nonlinear Mass Transport and Exchange in Biological Media. Seattle: University of Washington, Ph.D. Dissertation, 1995.
26. Richtmyer, R. D., and K. W. Morton. Difference Methods for Initial-Value Problems. New York: Interscience Publishers, 1967.
27. Roache, P. J. Computational Fluid Dynamics. Albuquerque, NM: Hermosa Publishers, 1972.

28. Rowlett, R. D., and T. R. Harris. A comparative study of organ models and numerical techniques for the evaluation of capillary permeability from multiple indicator-dilution data. *Math. Biosci.* 29:273–298, 1976.

NOMENCLATURE

$\mathbf{A}$, a_{ij} = matrix, matrix elements in Fourier analysis
$\mathbf{B}$ = differential operator in Eq. 11
C = concentration nmol · ml^{-1}
Co = Courant number, $u\,\Delta t/\Delta x$
D = axial diffusion coefficient (cm^2 · sec^{-1})
E = extraction ratio, $1 - C_p(L,t)/C_{ref}(L,t)$
F = flow rate of plasma (ml min^{-1} · g^{-1})
G = reaction rate (nmol min^{-1} · g^{-1})
$\mathbf{G}$ = amplification matrix in Fourier analysis
H = interpolation function
i = node index
$\mathbf{I}$ = identity matrix
I^2 = $= -1$
$k^{\pm}$ = reaction rate in binding reaction (min^{-1})
k = integer in random choice method
K_s = affinity constant for reaction rate, Eq. 5 (nmol · ml^{-1})
K'_{m_r} = affinity constant for transport rate, $r = p$ or c (nmol · ml^{-1})
L = length of capillary (cm)
M = maximum quantity in interpolation method
m = minimum quantity in interpolation method
n = number of time steps
N_{seg} = number of spatial segments
p_{+1} = rate at which the transporter-substrate complex flips or translocates the substrate binding site in the direction from plasma to cell and from cell to plasma, respectively (min^{-1})
p_{+0} = rate at which the free transporter flips or translocates the substrate binding site in the direction from plasma to cell and from cell to plasma, respectively (min^{-1})
PS = permeability-surface area product (ml min^{-1} · g^{-1})
RHS = right-hand side in interpolation method, Eq. 13
q = total moles (nmol)
S = substrate molecule
t = time (min)
T = free transporter molecule
T = surface concentration of free transporter (nmol · g^{-1})
TS = transporter-substrate complex
TC = surface concentration of transporter-substrate complex (nmol · g^{-1})
u = velocity of plasma (cm · min^{-1})
V_r = volume of distribution in region r ($r = c$ or p) (ml · g^{-1})
V_{max} = maximum rate of metabolism for reaction rate after Michaelis-Menten kinetics (ml · g^{-1})
V'_{max_r} = maximum rate of transport in transport rate after Michaelis-Menten kinetics ($r = p$ or c) (nmol · g^{-1} · min^{-1})
x = axial location (cm)

Greek symbols

γ = parameter in transport reaction (min^{-1})
δ = parameter in transporter reaction
ξ = Fourier variable; location in moving mesh
λ = eigenvalues of amplification matrix
κ = K_{s_c}/K_{s_p}
Γ = scaling factor in time-step limitation

Subscripts

c = intracellular region
$c \rightarrow p$ = intracellular region to plasma
ex = exact value
in = inlet value
n = number of time step
num = numerical solution
out = outlet value
p = plasma region
$p \rightarrow c$ = plasma to intracellular region
r = generic, = p or c
ref = reference
sub = substrate
t = total
T = total transporter sites
0 = initial value at time 0

Superscripts

* = tracer concentration
tot = total
~ = intermediate quantity
^ = Fourier coefficient